



Electrical Conductivity of Halide Perovskites Follows Expectations from Classical Defect Chemistry

Nico Leupold⁺,^[a] Anna Lena Seibel⁺,^[a] Ralf Moos,^{*[a]} and Fabian Panzer^{*[b]}

Defect chemistry is key to understand electrical properties of many functional materials including halide perovskites. However, expectations from defect chemistry about the dependency of defect densities on the doping regime of halide perovskites have not yet been clearly confirmed experimentally. Here, we measure the electrical conductivity of the model halide perovskite Methylammonium Lead Iodide over a wide range of iodine partial pressures. We find that with iodine partial pressure the electrical conductivity changes with different slopes in a double-logarithmic representation, indicating changes of the perovskite conductivity mechanism. Considering differences in the mobilities of the various defect species, we derive expectations about the dependence of the total

conductivity of the perovskite as a function of iodine partial pressure. We find iodine vacancies dominating the conductivity at low iodine partial pressures, whereas at higher partial pressures holes govern the total conductivity. We find the concentration of iodide vacancies to be $\sim 10^{18} \text{ cm}^{-3}$, in good agreement with the expected values based on intrinsic ionic disorder. Finally, for the case that the intrinsic ionic disorder concentration is overestimated, we elucidate the possibility to explain the conductivity profile by impurity induced acceptor doping in the perovskite. Thus, our work will allow to develop a more fundamental understanding about the electrical properties of halide perovskites.

Introduction

Within the past few years, halide perovskites have developed as promising semiconductor materials for the next generation of various (opto-)electronic devices.^[1] Regarding their electrical properties, halide perovskites differ significantly from classic inorganic or organic semiconductors as they exhibit a mixed conductivity with ionic and electronic contributions.^[2,3] The ionic conductivity in halide perovskites is due to the relatively high mobility of their halide ions, allowing for ion-migration upon applying an electric field.^[4,5] In some cases, ion migration is utilized to realize device concepts such as memristors or batteries.^[2,6] However, in applications such as perovskites based solar cells, X-ray detectors, or LEDs, ion migration leads to

efficiency losses and degradation,^[7] so that efforts were made to prevent these adverse effects.^[3]

It was found that, e.g., stoichiometry, grain orientation, processing conditions, additives, or changing the dimensionality of the perovskite impact the ionic conductivity.^[8] Furthermore, for the model halide perovskite Methylammonium Lead Iodide (MAPbI₃), ion migration can account for a large fraction of the total electrical conductivity both in the dark and under illumination.^[9,10]

In MAPbI₃, the presence of iodide vacancies allows for the migration of iodide, thus also iodide vacancies migrate.^[11,12] The latter are caused, for example, when an iodide ion at a regular lattice site moves to an interstitial site, leaving an iodide vacancy at the original iodide lattice site (referred to as (anion-) Frenkel defect).^[13] Alternatively, the formation of Schottky defects, which is the formation of a MA vacancy and an iodide vacancy, is well possible in MAPbI₃ and also results in the formation of iodide vacancies.^[12,14]

Iodide interstitials, iodide- or MA vacancies, all represent classical point defects that can widely determine the electrical transport behavior of halide perovskites.^[5] Accordingly, defect chemical modeling combined with appropriate characterization methods, offers a powerful way to gain in-depth understanding of the electrical conductivity in halide perovskites.^[13,15,16] Based on the defect chemical reactions that occur in the material, and by considering mass action laws, it is possible to derive so-called Kröger-Vink diagrams.^[17] They depict how the concentration of different defect species depends on the surrounding partial pressure of its chemical constituents. In the past, defect chemical modelling approaches were successfully used to understand and to design electrical properties of oxides for many electrical applications.^[18,19] The concentrations of the individual ionic- and electronic defects also correspond to the

[a] N. Leupold,⁺ A. L. Seibel,⁺ Prof. Dr. R. Moos
Department of Functional Materials,
University of Bayreuth,
Bayreuth 95440, Germany
E-mail: functional.materials@uni-bayreuth.de
<http://www.funktionsmaterialien.de/>

[b] Dr. F. Panzer
Soft Matter Optoelectronics, University of Bayreuth,
Bayreuth 95440, Germany
E-mail: fabian.panzer@uni-bayreuth.de
<https://www.ep2-bayreuth.de/perovskite-group/>

[⁺] Both authors contributed equally.

 Supporting information for this article is available on the WWW under <https://doi.org/10.1002/ejic.202100381>

 Part of the joint "Perovskite Materials and Devices" Special Collection with ChemPlusChem.

 © 2021 The Authors. European Journal of Inorganic Chemistry published by Wiley-VCH GmbH. This is an open access article under the terms of the Creative Commons Attribution License, which permits use, distribution and reproduction in any medium, provided the original work is properly cited.

density of mobile charge carriers. This allows to access the defect density experimentally by determining the electrical conductivity of the investigated sample.^[20] Maier and coworkers investigated the electrical conductivity of MAPbI₃ as a function of Na- or oxygen-doping, or by varying the iodine partial pressure $p(I_2)$.^[21–23] They found increasing electronic conductivity and concomitantly, slightly decreasing ionic conductivity with $p(I_2)$, both trends matching qualitatively with the expectation from the corresponding Kröger-Vink diagram.^[22] However, quantitatively, the conductivity changes with $p(I_2)$ deviated from the precise expectations from defect chemistry, suggesting that the perovskite was in a transition region between an intrinsic ionic and a p-type regime.^[22] Even though the previous studies demonstrated that investigating halide perovskites in the framework of defect chemistry allows for an understanding of different contributions to the electrical conductivity, it has not yet been shown that the experimentally determined conductivities precisely follow the expectations from defect chemical models across different distinct regimes in the Kröger-Vink diagrams.

Here, we measure the electrical conductivity of MAPbI₃ by impedance spectroscopy (IS) over a wide $p(I_2)$ range from $1.2 \cdot 10^{-10}$ bar to $3.2 \cdot 10^{-4}$ bar. This allows to experimentally identify different iodine partial pressure ranges, where the electrical conductivity exhibits different distinct slopes. Based on relatively simple defect chemical modeling, we derive Kröger-Vink diagrams and show how the iodine partial pressure dependent profiles of the defect concentrations correspond to the measured conductivity in a double-logarithmic representation. We further explain how conductivity vs. $p(I_2)$ curves can change depending on the ratio of the mobilities of the ionic and electronic defects. This finally allows to fully explain the measured conductivity profiles by means of defect chemical

models. Thus, our work demonstrates how defect chemistry can be used to thoroughly understand the conductivity properties of halide perovskites.

Results and Discussion

Figure 1 shows the scheme of the measurement setup, which is based on a carrier gas flow method.

The setup consists of a sublimation chamber (SC) connected with the measurement chamber (MC) via a tube. In the SC, dry nitrogen carrier gas flows through solid iodine crystals at a low flow rate of 0–0.2 l/min controlled by a mass flow controller (MFC). Iodine sublimates in the SC leading to a temperature dependent vapor pressure of iodine, $p(I_2)$. Assuming that the partial pressure of iodine in the sublimation chamber corresponds to its equilibrium vapor pressure at a specific temperature, the iodine vapor pressure can be calculated as given in literature (see equation S1).^[24]

Temperatures T_{SC} in the sublimation chamber ranging from –60 to 25 °C are achieved by surrounding cooling media, such as dry ice, ice and silicone oil. With that, vapor pressures from $1.5 \cdot 10^{-8}$ to $3.2 \cdot 10^{-4}$ bar can be realized in the SC. The tube that connects the SC and the MC is held at elevated temperatures to prevent iodine sublimation. Thus, it is possible to assume that the iodine partial pressure in the MC equals to the one in the SC. The MC and thus the MAPbI₃ sample are held at around 65 °C by using silicone oil as a heating media. To achieve an iodine partial pressure below $1.5 \cdot 10^{-8}$ bar, an additional nitrogen flow (0.2 to 10 l/min) is injected after the sublimation chamber to dilute the iodine saturated gas flow from the SC. To prevent uncontrolled cooling of the MC, the additional nitrogen flow is preheated to match the temperature of the (low flow

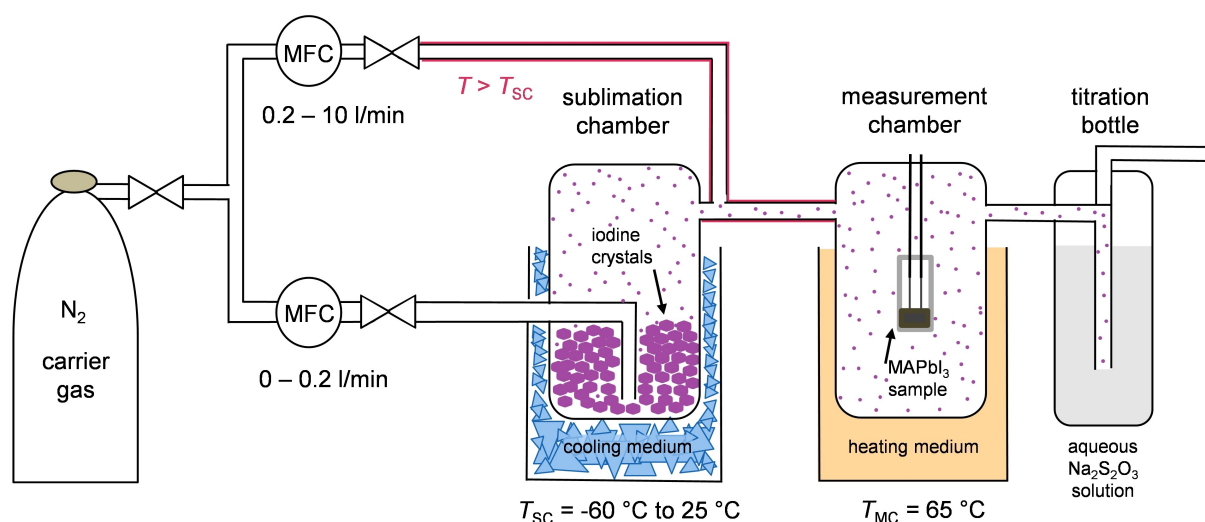


Figure 1. Schematic illustration of the setup used in this study to determine the electrical conductivity in a wide iodine partial pressure range between $1.6 \cdot 10^{-10}$ bar and $3.2 \cdot 10^{-4}$ bar at a sample temperature of $T_{MC} = 65$ °C. The setup consists of a sublimation chamber (SC), cooled by different cooling media (blue) and a sample measurement chamber (MC), heated by a heating medium (yellow). A nitrogen carrier gas (0–0.2 l/min), controlled by a mass flow controller (MFC), is passed through iodine crystals (purple) in the SC. Part of the iodine sublimates and forms a vapor, entering the MC in which the MAPbI₃ sample is located. For lower $p(I_2)$, a nitrogen flow for dilution (0.2–10 l/min) can be added between the SC and the MC. The iodine is neutralized afterwards with thiosulfate ions in an aqueous solution (grey), allowing for titration and thus quantitative validation of the $p(I_2)$.

rate) gas flow and the temperature of the MC. With that, it was possible to set the iodine partial pressure in the MC to values between $1.2 \cdot 10^{-10}$ bar and $3.2 \cdot 10^{-4}$ bar.

To validate the partial pressure of iodine, the outlet gas downstream of the measurement chamber was led into an aqueous $\text{Na}_2\text{S}_2\text{O}_3$ solution, where the iodine was dissolved. The total amount of iodine that has been flown through the setup was then determined by titration, allowing to calculate the iodine partial pressure retrospectively (see SI and Figure S1 for details).

The investigated MAPbI_3 sample consists of an Al_2O_3 substrate with interdigitated carbon electrodes on which the MAPbI_3 layer is processed (Figure S2). The electrodes have a height of $\sim 15 \mu\text{m}$. Due to the lateral electrode arrangement, a MAPbI_3 layer thickness in the same range as the electrode height is desired, to reduce the measured resistance values and thus improve the overall signal to noise ratio.

Therefore, we used the dry Powder Aerosol Deposition Method (PADM) to produce polycrystalline MAPbI_3 layers with suitable thickness in the range of the carbon electrode height. PADM has been used in the past in the field of ceramics and perovskites to produce dense and thick, polycrystalline layers based on dry source powders at room temperature.^[25] As source powders we used mechanochemically synthesized MAPbI_3 powder (see the experimental section and Ref. [26] for details about the synthesis route). Flowing N_2 gas through the MAPbI_3 powder created a dry aerosol that was fed into the deposition chamber via a nozzle. Driven by a pressure gradient between the nozzle and the evacuated deposition chamber, the aerosol accelerated toward the Al_2O_3 substrate. Upon impacting on the substrate with high kinetic energy, the MAPbI_3 powder particles adhere to the substrate. With that it was possible to produce a $30 \mu\text{m}$ thick MAPbI_3 layer (see Figure S3 for details). PADM processed halide perovskite layers typically exhibit a relatively large surface roughness, which potentially accelerates the equilibration with the surrounding iodine atmosphere. This reduces the measurement time, which in turn is beneficial in terms of sample degradation and reproducibility. The tetragonal crystal structure of the MAPbI_3 powder is maintained in the PAD-film as evidenced from XRD (Figure S4). Furthermore, the absence of additional signals in the diffractogram of the PADM-processed sample compared to the powder XRD indicates that the MAPbI_3 layers are phase-pure. Besides that, the reflexes in the XRD pattern of the layer are slightly broader compared to the corresponding reflexes of the powder, suggesting a reduction of the crystallite size due to the PADM.

The electrical conductivity of the MAPbI_3 samples was determined by impedance spectroscopy (IS) between 1 Hz and 10 MHz. The IS spectra were fitted with an equivalent circuit, consisting of two RC parallel elements and a Warburg element. The electrical conductivity, σ , was calculated by taking into account the dominating resistor, the geometry of the electrodes and the layer thickness (see Figures S2 and S5 for details). Since exposing halide perovskites to light and air can have a significant influence on their conductivity,^[27] all measurements were conducted in darkness and in a dry and oxygen-free nitrogen atmosphere.

Figure 2 shows the electrical conductivity as a function of the iodine partial pressure in the range of $1.2 \cdot 10^{-10}$ to $3.2 \cdot 10^{-4}$ bar, plotted in a double logarithmic representation. Beside the conductivity values from a first series of measurements (dark grey squares), also the values from a second series of measurements (red dots), which was carried out two weeks later, are plotted. There are no significant differences between the data from the two measurement-series, demonstrating the high reproducibility of the measurement conditions, and the good reversibility of the iodine incorporation and removal. This is in line with results from literature, where no permanent change in conductivity was observed upon exposing MAPbI_3 to iodine partial pressures $< 10^{-5}$ bar.^[22,23] In Figure 2, three ranges can be identified in which the change of conductivity with iodine partial pressure exhibits different slopes. From 10^{-10} to approx. 10^{-7} bar iodine partial pressure, the electrical conductivity is constant at approximately $2 \cdot 10^{-8}$ S/cm. When $p(\text{I}_2)$ increases to $6.4 \cdot 10^{-5}$ bar, the electrical conductivity increases significantly to about $5.3 \cdot 10^{-7}$ S/cm. In the double logarithmic representation, this corresponds to an increase in conductivity with a slope of about $1/2$. When the iodine partial pressure further increases to $3.2 \cdot 10^{-4}$ bar, the conductivity increases to $7.8 \cdot 10^{-7}$ S/cm corresponding to a slope of about $1/4$. However, the accuracy of this slope value is limited here due to the small number of data points.

In the following, we derive how the dependence of the conductivity on the iodine partial pressure observed in Figure 2 can be understood using simple defect chemical modelling. For this purpose, we use the Kröger-Vink notation,^[28] where V_i^+ and V_{MA}^- denote positively charged iodide vacancies or negatively charged MA vacancies, respectively. Square brackets in the mass action laws indicate the concentration of the respective defect species. As mentioned earlier, ionic defects in MAPbI_3 can in principle result from Schottky or Frenkel disorder.^[12–14] However, at the moment no clear consensus regarding the dominant disorder type in MAPbI_3 has evolved yet.^[4,13,14,16,29,30] Nevertheless, as Schottky disorder in MAPbI_3 was suggested to have a relatively low formation enthalpy of ~ 0.1 eV,^[14] we consider Schottky disorder in the following defect chemical considerations (see SI for defect chemical modelling considering Frenkel disorder).

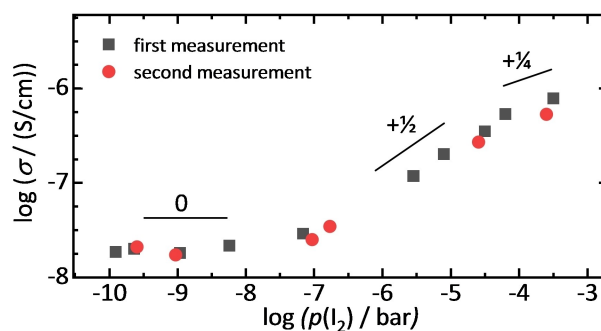


Figure 2. Electrical conductivity as a function of iodine partial pressure of powder aerosol deposited MAPbI_3 films calculated from impedance spectra.

In the case of Schottky disorder, the associated defect chemical reaction and the associated mass action law with the equilibrium constant K_s read:



$$K_s = [V_{MA}^{\cdot}] \cdot [V_i^{\cdot}] \quad (2)$$

This means, MA^+ and I^- leave their regular lattice sites, creating negatively charged MA vacancies and positively charged iodide vacancies and forming an additional MAI molecule. A change in the iodine partial pressure shifts the chemical equilibrium between the perovskite and the gas phase and thus the point defect concentrations in the perovskite. With increasing iodine partial pressure, iodide vacancies are filled, also leading to the formation of defect electrons (holes) h^* to maintain the overall charge balance. This corresponds to acceptor (p-type) doping at high iodine partial pressures.^[31]



The associated mass action law determines the equilibrium concentrations of iodine sites and of holes, depending on the iodine partial pressure $p(I_2)$. The concentration of the holes $[h^*]$ is abbreviated with p and it follows:

$$K_{Ox} = p \cdot p(I_2)^{-\frac{1}{2}} \cdot [V_i^{\cdot}]^{-1} \quad (4)$$

In addition, the intrinsic electronic disorder (generation and recombination of electron-hole pairs) and the associated mass action law must be considered, where the concentration of electrons $[e^-]$ is abbreviated as n :



$$K_i = n \cdot p \quad (6)$$

From the outside, the perovskite is neutral, and accordingly the electroneutrality condition must be fulfilled, i.e., the sum of the concentrations of all negative charge carriers must be equal to the sum of concentrations of all positive charge carriers:

$$n + [V_{MA}^{\cdot}] = p + [V_i^{\cdot}] \quad (7)$$

Figure 3a shows the Kröger-Vink diagram depicting the dependencies of the concentrations of the different defect species on the iodine partial pressure derived from equations 1–7 (see SI for more details). In passing, we note that the defect chemical considerations can also be carried out analogously for an anion-Frenkel disorder (I^- leaves its regular lattice site, goes to an interstitial site, while leaving an I^- vacancy; see SI for details). Depending on whether a Schottky disorder or an anion-Frenkel disorder is assumed, the dashed blue line in Figure 3 represents either the concentration profile of methylammonium vacancies V_{MA}^{\cdot} (Schottky) or iodine interstitials I_i^{\cdot} (Frenkel). However, regardless which of the two types of

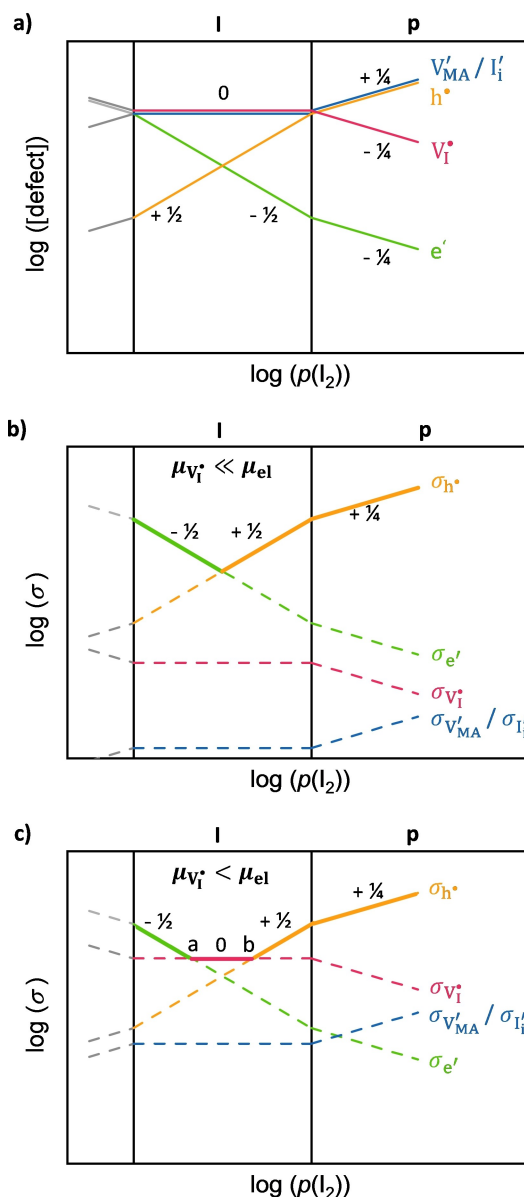


Figure 3. (a) Kröger-Vink diagram illustrating the dependence of defect concentration on the iodine partial pressure in the intrinsic and p-conducting regime. The dash-dotted blue line corresponds to V_{MA}^{\cdot} or I_i^{\cdot} depending on whether intrinsic Schottky or Anion-Frenkel disorder is assumed. The slopes for the different defect concentrations are indicated. (b), (c) Dependence of the conductivity of each species on the iodine partial pressure for (b) $\mu_{V_i^{\cdot}} \ll \mu_{eI}$ and (c) $\mu_{V_i^{\cdot}} < \mu_{eI}$. The solid lines show the dominant contribution to the total conductivity.

disorder is considered, the change of defect concentrations with iodine partial pressure remains the same. As it was suggested in literature to be the dominant effect responsible for the intrinsic disorder in halide perovskites,^[14,23] we consider Schottky disorder in the following.

In Figure 3a, an iodine partial pressure range is shown, in which the intrinsic ionic defects V_i^{\cdot} and V_{MA}^{\cdot} dominate the overall defect density (referred to as intrinsic regime I), i.e., in equation 7, n and p can be neglected. Accordingly, the electro-

neutrality condition in the I-regime simplifies to $[V_{MA}^{\bullet}] \approx [V_I^{\bullet}]$. From equation 2 follows:

$$[V_I^{\bullet}] = [V_{MA}^{\bullet}] = K_S^{\frac{1}{2}} \quad (8)$$

As long as $[V_{MA}^{\bullet}] \approx [V_I^{\bullet}]$ holds, the ionic defect concentrations are approximately independent of the iodine partial pressure within the I-regime. Substituting equation 8 into equation 4, then gives

$$p = K_{Ox} \cdot K_S^{\frac{1}{2}} \cdot p(I_2)^{\frac{1}{2}} \quad (9)$$

Thus, within the I-regime, p increases with iodine partial pressure, exhibiting a slope of $1/2$ in the double logarithmic representation. Complementary (equation 6), n decreases with a slope of $-1/2$.

At higher iodine partial pressure, the increasing concentration of holes reaches the same order of magnitude as the ionic defects. Then, changes in the ionic defect concentration due to filling of V_I^{\bullet} (also resulting in the formation of V_{MA}^{\bullet} (equation 2)) can no longer be neglected. As a result, a new regime starts where V_{MA}^{\bullet} and holes exhibit the highest defect concentrations. Then, the electroneutrality condition (equation 7) simplifies to $p \approx [V_{MA}^{\bullet}]$ in the corresponding iodine partial pressure range (referred to as p-regime). Using $p \approx [V_{MA}^{\bullet}]$, equations 2–6 allow to derive the changes of individual defect concentrations as a function of iodine partial pressure in the p-regime. Here, the concentration of V_{MA}^{\bullet} increases with a slope of $1/4$, and complementary to this (equation 2), $[V_I^{\bullet}]$ decreases. At the same time, p increases with a slope of $1/4$, while n decreases with a slope of $-1/4$ (see SI for details).

Based on the defect chemical considerations as described above, at very low partial pressures, we would expect MAPbI₃ to become n -conducting (referred to as n-regime) due to the dominant contribution of electrons to the total defect density. In this n-regime, a higher total conductivity would be expected in comparison to the I-regime. A change from p- to n-doping and an increase in total conductivity indeed could be observed by Maier et al., when immersing a MAPbI₃ layer in toluene, leading to a partial removal of iodine from the perovskite.^[10] In our experiments, we do not observe any increase of the conductivity towards the smallest iodine partial pressure of $1.2 \cdot 10^{-10}$ bar. Therefore, we conclude that for our MAPbI₃ layer, the I-regime and the beginning of the p-regime from the Kröger-Vink diagram are accessible experimentally within the iodine partial pressure range realized in this work.

Next, we focus on deriving the expected electrical conductivity behavior as a function of the iodine partial pressure, based on the Kröger-Vink diagram in Figure 3a. In general, the total electrical conductivity σ_{tot} of a semiconductor is the sum of all electronic contributions σ_{el} and ionic contributions σ_{ion} , i.e., $\sigma_{tot} = \sigma_{el} + \sigma_{ion}$. The electronic conductivity is determined by the product of the charge carrier density, the mobility μ for electrons and holes, respectively, and the elementary charge e , i.e., $\sigma_{el} = \mu_e \cdot n \cdot e + \mu_h \cdot p \cdot e$. In ionic conduction, ions i with a concentration $[i]$ move via hopping across interstitials or vacancies. To calculate the ionic conductivity of a particular ion

species, its valence $|z_i|$ and its mobility μ_i must be considered. The total ionic conductivity is obtained as the sum of the contributions from each individual ion species i to $\sigma_{ion} = \sum_i |z_i| \cdot \mu_i \cdot [i] \cdot e$. Assuming that the charge carriers do not interact with each other, the concentrations of the various electronic and ionic charge carriers for each partial pressure can be obtained from the Kröger-Vink diagram. We further assume that the mobilities of the different carrier species are constant over the investigated iodine partial pressure range. Then, the qualitative characteristics (i.e., the slopes) of the individual defect concentrations as a function of iodine partial pressure directly lead to the qualitative characteristics of corresponding conductivities. Compared to the positions in the Kröger-Vink diagram, the positions of the individual conductivities in the $\sigma(p(I_2))$ -diagram are shifted vertically, depending on the mobilities of the different charge carrier species.

In the case of MAPbI₃ the mobilities of electrons and holes are typically found to exhibit values in the same range,^[32] so that we can assume $\mu_{el} = \mu_e = \mu_h$. When it comes to the conductivities of the ions, it was found that $\mu_{V_{MA}^{\bullet}}$ is about three orders of magnitude lower than $\mu_{V_I^{\bullet}}$.^[22] Therefore, the contribution of V_{MA}^{\bullet} to the conductivity is shifted towards lower values than the contribution of V_I^{\bullet} by a certain amount, depending on the exact difference between $\mu_{V_{MA}^{\bullet}}$ and $\mu_{V_I^{\bullet}}$. In the following we assume that the magnitude of the shift between $\sigma_{V_{MA}^{\bullet}}$ and $\sigma_{V_I^{\bullet}}$ is always the same and that $\mu_{V_{MA}^{\bullet}}$ is always significantly lower than μ_{el} .

If the V_I^{\bullet} (and all the more V_{MA}^{\bullet}) are nearly immobile compared to the electrical defects, i.e., $\mu_{V_I^{\bullet}} \ll \mu_{el}$, the conductivity of the ions is significantly lower than the conductivity of the electrons and holes (Figure 3b), even though the concentrations of the ionic defects in the Kröger-Vink diagram (Figure 3a) were higher than or equal to the concentrations of the electronic charge carriers (Figure 3a). For $\mu_{V_I^{\bullet}} \ll \mu_{el}$, the electronic defects are the dominant contribution to the electrical conduction σ_{tot} throughout the entire iodine partial pressure range investigated (see solid lines in Figure 3b). A typical so-called intrinsic conductivity minimum appears, a behavior that can be seen in many oxide ceramics when the oxygen partial pressure is varied.^[18,20]

An increase in the ionic mobility relative to the electronic mobility shifts the contributions of the V_I^{\bullet} and V_{MA}^{\bullet} to higher values in the conductivity diagram. Figure 3c shows a conductivity diagram with μ_{ion} higher than the one in Figure 3b, but still $\mu_{V_I^{\bullet}} < \mu_{el}$. At low partial pressures, electrons are the dominant contribution to the total conduction, where n decreases with increasing iodine partial pressure with a slope of $-1/2$, analogous to Figure 3b. However, due to the increased conductivities of the ionic species, the V_I^{\bullet} become the dominant contribution to the total conductivity above a certain iodine partial pressure (point "a" in Figure 3c). Accordingly, the total conductivity remains constant over a certain iodine partial pressure range, before the increasing hole conductivity becomes the dominant contribution to the total conductivity (referred to as point 'b' in Figure 3c). From point 'b' onwards, the total conductivity increases with a slope of $1/2$ and increases with a slope of $1/4$ at even higher iodine partial pressures,

analogous to the case shown in Figure 3b. Even though in reality the cases $\mu_{V_I^*} \approx \mu_{el}$ or even $\mu_{V_I^*} > \mu_{el}$ are not expected for MAPbI₃,^[22,32] for completeness the corresponding conductivity diagrams are shown in the SI (Figure S6).

In Figure 2, we observed that for increasing iodine partial pressures the total conductivity of our sample was first constant, then increased with a slope of $1/2$ and thereafter with a slope of $1/4$. This experimentally determined conductivity profile agrees with the profile derived on the basis of defect chemistry modeling, for $\mu_{V_I^*} < \mu_{el}$ (Figure 3c). This is in line with the fact that in MAPbI₃, the mobilities of the ionic defects V_I^* and V_{MA} are found to be significantly lower ($\mu_{V_I^*} \approx 5 \cdot 10^{-8} \text{ cm}^2 \text{ V}^{-1} \text{ s}^{-1}$ and $\mu_{V_{MA}} \approx 8 \cdot 10^{-11} \text{ cm}^2 \text{ V}^{-1} \text{ s}^{-1}$ at 70 °C),^[22] than the corresponding electronic mobilities (0.4–35 $\text{cm}^2 \text{ V}^{-1} \text{ s}^{-1}$).^[32] Accordingly, we conclude that in the range in Figure 2, where the conductivity is constant, the electrical conductivity is dominated by the iodide vacancies, and in the range with slope $1/2$ and $1/4$, it is dominated by the holes. In general, the intrinsic value of $[V_I^*]$ in MAPbI₃ at a certain temperature T , can be estimated by^[29]

$$[V_I^*] = [I_i^*] \cdot \exp\left(-\frac{E_{DF}}{k_B T}\right) \quad (10)$$

with E_{DF} being the defect formation energy of a charged iodide vacancy, and $[I_i^*]$ corresponding to the concentration of iodine in MAPbI₃. As three iodine are present per MAPbI₃ unit cell, and the latter has a volume V of $\sim 252 \text{ \AA}^3$ in the cubic crystal structure,^[33] we estimate $[I_i^*] = 3/V = 1.2 \cdot 10^{22} \text{ cm}^{-3}$. The reported defect formation energies of iodide vacancies in MAPbI₃ spread between 0.08 and 0.8 eV,^[14,29,30,34] resulting in a wide range of values for $[V_I^*]$ from $1.4 \cdot 10^{10}$ to $7.7 \cdot 10^{20} \text{ cm}^{-3}$.

The measured conductivity in the I-regime in Figure 2 yields a value of $\sigma_{tot} = \sigma_{ion} \approx 2 \cdot 10^{-8} \text{ S cm}^{-1}$. Using $\sigma_{ion} = \sum_i |z_i| \cdot \mu_i \cdot [i] \cdot e$ and $\mu_{V_I^*} = 5 \cdot 10^{-8} \text{ cm}^2 \text{ V}^{-1} \text{ s}^{-1}$,^[22] a concentration of iodide vacancies $[V_I^*] = 2.5 \cdot 10^{18} \text{ cm}^{-3}$ follows. This value agrees well with the range of literature-based values calculated using equation 10, nicely demonstrating that the relatively simple defect chemical model derived above is capable of explaining the electrical properties of the halide perovskite. Furthermore, the relatively high iodide vacancy concentration in the range of 10^{18} cm^{-3} suggests that ion migration might also occur in the MAPbI₃ powder that we used to process the PADM samples. Indeed, in pressed pellets based on mechanochemically synthesized perovskite powders, which should closely resemble the neat powder properties, the presence of ion migration has already been demonstrated in the past.^[26,35]

However, it is also clear that due to the wide range of $[V_I^*]$ derived from the E_{DF} values, it might be also possible that the intrinsic concentration of the iodide vacancies is below 10^{18} cm^{-3} in MAPbI₃. Then, our measured values of σ_{tot} could no longer be fully explained with the help of the simple defect chemical model developed above. Instead, in the iodine partial pressure range, which was referred to as I-regime before, an additional acceptor doping A' of the perovskite with $[A'] = 2.5 \cdot 10^{18} \text{ cm}^{-3}$, would need to be considered. Acceptors are

impurities that have a lower valence than the replaced ion in the host lattice, so that negative charge is introduced into the perovskite. However, the charge neutrality condition still applies, now reading:

$$n + [V_{MA}] + [A'] = p + [V_I^*] \quad (11)$$

Thus, the concentration of iodide vacancies and/or holes must increase to compensate for the additional charge of the acceptor. Since in MAPbI₃ the ionic defects outnumber the electronic defects in the intrinsic regime,^[30] it can be assumed that the charge of the acceptors is compensated by the formation of additional iodide vacancies.

Accordingly, following equation 2, the concentration of V_{MA} decreases and equation 11 becomes $[A'] \approx [V_I^*]$. Since the concentration of the acceptors is independent of the iodine partial pressure, also the concentration of the iodide vacancies remains constant within this regime. Analogous to the approach above, the concentration of the holes in the iodine partial pressure range in which $[A'] \approx [V_I^*]$ holds, is obtained by substituting the simplified electroneutrality condition into equation 4 resulting in

$$p = K_{ox} \cdot [A'] \cdot p(I_2)^{1/2} \quad (12)$$

This means that even if an acceptor concentration that is higher than the intrinsic ionic defect concentration is present in the perovskite, the total conductivity again exhibits an iodine partial pressure dependent profile which at first is constant, and then increases with a slope of $1/2$ in the case of $\mu_{V_I^*} < \mu_{el}$. With increasing iodine partial pressure, the concentration of the holes increases further until it reaches the same order of magnitude as the concentration of the iodide vacancies and the simplification of the electroneutrality condition of $[A'] \approx [V_I^*]$ no longer applies.

Rather, the holes then represent the defect species with the highest concentration, which counterbalance the charge of the acceptors. Consequently, equation 11 simplifies to $[A'] \approx p$. In the iodine partial pressure regime where the latter assumption holds, it follows from the independence of $[A']$ from the iodine partial pressure that the slope of total conductivity is 0.^[23] The flattening of the slope of the measured conductivity toward the highest iodine partial pressures investigated in Figure 2, would then indicate reaching the transition region from $[A'] \approx [V_I^*]$ to $[A'] \approx p$. Overall, it becomes clear that in the case of $[V_I^*]$ well below 10^{18} cm^{-3} , the conductivity profile measured in Figure 2 can also be fully explained by the presence of acceptor impurities with $[A'] = 2.5 \cdot 10^{18} \text{ cm}^{-3}$. In this case, one would expect a conductivity that increases linearly with the acceptor concentration in the range where the conductivity is constant. This should be evaluated in future studies. Based on the results about the dependence of the electrical properties on defects presented here, it will be also interesting in the future to investigate the influence of the iodine partial pressure on the optoelectronic properties of halide perovskites.

Conclusion

In this work, we investigated the electrical conductivity σ of MAPbI₃ films fabricated by PADM over a wide $p(I_2)$ range from $1.2 \cdot 10^{-10}$ bar to $3.2 \cdot 10^{-4}$ bar. We identified three iodine partial pressure ranges where the change of conductivity with iodine partial pressure subsequently exhibits slopes of 0, $\frac{1}{2}$ and $\frac{1}{4}$ in the double logarithmic representation of the $\sigma(p(I_2))$ -diagram. To understand the conductivity profile, we derived Kröger-Vink diagrams based on relatively simple defect chemical models. Depending on the ratio of the mobilities of the ionic and electronic defects we showed, how the iodine partial pressure dependent profiles of the defect concentrations translate to the corresponding profile of the measured conductivity. In the framework of our defect chemical considerations, we find that in the range with constant conductivity, iodide vacancies are the dominant charge carriers with a concentration of $[V_i^*] = 2.5 \cdot 10^{18} \text{ cm}^{-3}$. They can be caused by an intrinsic Schottky- or Frenkel-disorder or by an impurity induced acceptor doping. At higher iodine partial pressures, holes dominate the conductivity with slopes of $\frac{1}{2}$ and $\frac{1}{4}$. Our work demonstrates how defect chemical considerations can be used to better understand the conductivity properties of halide perovskites.

Experimental Section

Setup for Iodine Partial Pressure Control: Mainly PTFE and borosilicate glass are used, as the setup needs to be gas-tight and corrosion-resistant to iodine even at elevated temperatures. It also ensures that no iodine is lost, especially at low iodine partial pressures, by chemical reactions with the apparatus. To prevent accidental doping with the carrier gas, nitrogen with a purity of 99.999% was used. The iodine crystals in the sublimation chamber had a purity of 99.8% (Carl Roth). The sample temperature was 65 °C during the conductivity measurements.

Powder Synthesis: For synthesis of the MAPbI₃ powder, 1.9 g methylammonium iodide (CH₃NH₃I) and 5.509 g lead iodide (PbI₂, TCI) were weighed under ambient conditions into zirconia milling jars containing 25 zirconia milling balls (10 mm diameter). 5 ml cyclohexane was added as a milling agent. For milling, a Fritsch "Pulverisette 5/4" planetary ball mill at a rotational speed of 400 rpm was used. The total milling time was 25 min with pauses every 5 min for 20 min to cool down the jar. After evaporating the cyclohexane in air, the powder was sieved (mesh size 63 μm).

Powder Aerosol Deposition Method: The samples were produced via powder aerosol deposition method (PADM), where nitrogen was used as a carrier gas (8.5 l/min). Before deposition, the powder was dried at 120 °C for 1 h. For deposition, 1 g of powder, a scan rate of 1 mm/s and a substrate-to-nozzle distance of 3 mm was used. The total area of $10 \times 13 \text{ mm}^2$ was scanned 60 times. The processing parameters are summarized in Table S1 and Figure S3 shows a scheme of the apparatus for the Powder Aerosol Deposition of thick MAPbI₃-films.

Sample Geometry: Alumina (96% purity) with a screen-printed interdigitated carbon electrode with 29 fingers of 4 mm length, 107 μm width and 100 μm spacing was used as the substrate. The area of charge carrier transport A of the interdigital electrode (IDE) was calculated via equation S3 and the geometry with typical metrics of the electrode is visualized in Figure S2.

XRD: The structural and phase characterization of the perovskite powders and films was carried out by reflection mode XRD using a Bruker "D8 Discover A25" with Cu-K α -radiation ($\lambda = 0.15406 \text{ nm}$). The K α -rays are removed by a Ge-K α -monochromator and the device is operated at 40 kV and 40 mA. The diffractograms were recorded in the 2θ range from 10 to 45° with a 2θ step size of 0.016°.

Impedance Spectroscopy: The electric behavior of MAPbI₃ was observed by impedance spectroscopy. For the two-wire measurements an Alpha-A High Performance Frequency Analyzer from the manufacturer Novocontrol Technologies was used. To avoid timely drifts a DC voltage of 0.5 V was applied for 15 minutes. For the subsequent measurements, an AC voltage with an amplitude of 30 mV was added to the DC bias of 0.5 V. The frequency was varied from 10 MHz to 1 Hz.

Acknowledgements

The authors acknowledge financial support by the German National Science Foundation DFG via the projects PA 3373/3-1 and MO 1060/32-1. We further thank Irene Bauer for MAI synthesis, Monika Daubinger for powder synthesis and assistance with the titrimetry, Daniel Lukas for powder aerosol deposition of the samples and the Department of Metal and Alloys (Prof. Dr. Uwe Glatzel) for the possibility to conduct XRD measurements. Open access funding enabled and organized by Projekt DEAL.

Conflict of Interest

The authors declare no conflict of interest.

Keywords: Iodine partial pressure · Doping · Ion migration · MAPbI₃ · Impedance Spectroscopy · Powder aerosol deposition method

- [1] a) J. Y. Kim, J.-W. Lee, H. S. Jung, H. Shin, N.-G. Park, *Chem. Rev.* **2020**, *120*, 7867; b) K. Ji, M. Anaya, A. Abfalterer, S. D. Stranks, *Adv. Opt. Mater.* **2021**, 2002128; c) G. Kakavelakis, M. Gedda, A. Panagiotopoulos, E. Kymakis, T. D. Anthopoulos, K. Petridis, *Adv. Sci.* **2020**, *7*, 2002098.
- [2] W. Tress, *J. Phys. Chem. Lett.* **2017**, *8*, 3106.
- [3] M. H. Futscher, J. V. Milić, *Front. Energy Res.* **2021**, *9*, 629074.
- [4] A. Senocrate, J. Maier, *J. Am. Chem. Soc.* **2019**, *141*, 8382.
- [5] A. Walsh, S. D. Stranks, *ACS Energy Lett.* **2018**, *3*, 1983.
- [6] a) F. Ma, Y. Zhu, Z. Xu, Y. Liu, X. Zheng, S. Ju, Q. Li, Z. Ni, H. Hu, Y. Chai, C. Wu, T. W. Kim, F. Li, *Adv. Funct. Mater.* **2020**, *30*, 1908901; b) S. Ahmad, C. George, D. J. Beesley, J. J. Baumberg, M. de Volder, *Nano Lett.* **2018**, *18*, 1856; c) L. Zhang, J. Miao, J. Li, Q. Li, *Adv. Funct. Mater.* **2020**, *30*, 2003653; d) S. Narayanan, N. Parikh, M. M. Tavakoli, M. Pandey, M. Kumar, A. Kalam, S. Trivedi, D. Prochowicz, P. Yadav, *Eur. J. Inorg. Chem.* **2021**, 2021, 1201.
- [7] a) J. Carrillo, A. Guerrero, S. Rahimnejad, O. Almora, I. Zarazua, E. Mas-Marza, J. Bisquert, G. Garcia-Belmonte, *Adv. Energy Mater.* **2016**, *6*, 1502246; b) C. Li, A. Guerrero, Y. Zhong, S. Huettner, *J. Phys. Condens. Matter* **2017**, *29*, 193001.
- [8] a) S. Bai, P. Da, C. Li, Z. Wang, Z. Yuan, F. Fu, M. Kawecki, X. Liu, N. Sakai, J. T.-W. Wang, S. Huettner, S. Buecheler, M. Fahiman, F. Gao, H. J. Snaith, *Nature* **2019**, *571*, 245; b) P. Fassel, S. Ternes, V. Lami, Y. Zakharko, D. Heimfarth, P. E. Hopkinson, F. Paulus, A. D. Taylor, J. Zausseil, Y. Vaynzof, *ACS Appl. Mater. Interfaces* **2019**, *11*, 2490; c) Z. Huang, A. H. Proppe, H. Tan, M. I. Saidaminov, F. Tan, A. Mei, C.-S. Tan, M. Wei, Y. Hou, H. Han, S. O. Kelley, E. H. Sargent, *ACS Energy Lett.* **2019**, *4*, 1521;

- d) S. Reichert, Q. An, Y.-W. Woo, A. Walsh, Y. Vaynzof, C. Deibel, *Nat. Commun.* **2020**, *11*, 6098; e) P. Fassl, V. Lami, A. Bausch, Z. Wang, M. T. Klug, H. J. Snaith, Y. Vaynzof, *Energy Environ. Sci.* **2018**, *11*, 3380.
- [9] T.-Y. Yang, G. Gregori, N. Pellet, M. Grätzel, J. Maier, *Angew. Chem. Int. Ed.* **2015**, *54*, 7905.
- [10] G. Y. Kim, A. Senocrate, T.-Y. Yang, G. Gregori, M. Grätzel, J. Maier, *Nat. Mater.* **2018**, *17*, 445.
- [11] a) C. Eames, J. M. Frost, P. R. F. Barnes, B. C. O'Regan, A. Walsh, M. S. Islam, *Nat. Commun.* **2015**, *6*, 7497; b) J. M. Azpiroz, E. Mosconi, J. Bisquert, F. de Angelis, *Energy Environ. Sci.* **2015**, *8*, 2118.
- [12] Y. Yuan, J. Huang, *Acc. Chem. Res.* **2016**, *49*, 286.
- [13] D. Barboni, R. A. De Souza, *Energy Environ. Sci.* **2018**, *11*, 3266.
- [14] A. Walsh, D. O. Scanlon, S. Chen, X. G. Gong, S.-H. Wei, *Angew. Chem. Int. Ed.* **2015**, *54*, 1791.
- [15] D. Moia, J. Maier, *ACS Energy Lett.* **2021**, 1566.
- [16] R. A. De Souza, D. Barboni, *Chem. Commun.* **2019**, 55, 1108.
- [17] J. Maier, *Physical Chemistry of Ionic Materials. Ions and Electrons in Solids*, Wiley, Chichester, **2004**.
- [18] R. Moos, K. H. Härdtl, *J. Am. Ceram. Soc.* **1997**, *80*, 2549.
- [19] a) F. Gunkel, S. Hoffmann-Eifert, R. Dittmann, S. B. Mi, C. L. Jia, P. Meuffels, R. Waser, *Appl. Phys. Lett.* **2010**, *97*, 12103; b) R. Merkle, J. Maier, *Angew. Chem. Int. Ed.* **2008**, *47*, 3874; c) R. A. Maier, C. A. Randall, *J. Am. Ceram. Soc.* **2016**, *99*, 3350; d) T. Baiatu, R. Waser, K.-H. Härdtl, *J. Am. Ceram. Soc.* **1990**, *73*, 1663.
- [20] D. M. Smyth, *The defect chemistry of metal oxides*, Oxford University Press, New York, **2000**.
- [21] A. Senocrate, T. Acartürk, G. Y. Kim, R. Merkle, U. Starke, M. Grätzel, J. Maier, *J. Mater. Chem. A* **2018**, *6*, 10847.
- [22] A. Senocrate, I. Moudrakovski, G. Y. Kim, T.-Y. Yang, G. Gregori, M. Grätzel, J. Maier, *Angew. Chem. Int. Ed.* **2017**, *56*, 7755.
- [23] A. Senocrate, T.-Y. Yang, G. Gregori, G. Y. Kim, M. Grätzel, J. Maier, *Solid State Ionics* **2018**, *321*, 69.
- [24] L. J. Gillespie, L. H. D. Fraser, *J. Am. Chem. Soc.* **1936**, *58*, 2260.
- [25] a) J. Akedo, *J. Therm. Spray Technol.* **2008**, *17*, 181; b) F. Panzer, D. Hanft, T. Gujar, F.-J. Kahle, M. Thelakkat, A. Köhler, R. Moos, *Materials* **2016**, *9*, 277; c) M. Schubert, D. Hanft, T. Nazarenius, J. Exner, M. Schubert, P. Nieke, P. Glosse, N. Leupold, J. Kita, R. Moos, *Funct. Mater. Lett.* **2019**, *12*, 1930005; d) J. Akedo, *J. Ceram. Soc. Jpn.* **2020**, *128*, 101; e) N. Leupold, F. Panzer, *Adv. Funct. Mater.* **2021**, *31*, 2007350; f) J. Exner, T. Nazarenius, D. Hanft, J. Kita, R. Moos, *Adv. Mater.* **2020**, *32*, e1908104.
- [26] N. Leupold, K. Schötz, S. Cacovich, I. Bauer, M. Schultz, M. Daubinger, L. Kaiser, A. Rebai, J. Rousset, A. Köhler, P. Schulz, R. Moos, F. Panzer, *ACS Appl. Mater. Interfaces* **2019**, *11*, 30259.
- [27] a) M. A. Haque, A. Syed, F. H. Akhtar, R. Shevate, S. Singh, K.-V. Peinemann, D. Baran, T. Wu, *ACS Appl. Mater. Interfaces* **2019**, *11*, 29821; b) M.-A. Stoeckel, M. Gobbi, S. Bonacchi, F. Liscio, L. Ferlauto, E. Orgiu, P. Samorì, *Adv. Mater.* **2017**, 29.
- [28] F. A. Kröger, H. J. Vink in *Solid State Physics* (Eds.: F. Seitz, D. Trunbull), Academic Press, New York, **1956**, pp. 307–435.
- [29] D. Meggiolaro, E. Mosconi, F. de Angelis, *ACS Energy Lett.* **2019**, *4*, 779.
- [30] W. Ming, S. Chen, M.-H. Du, *J. Mater. Chem. A* **2016**, *4*, 16975.
- [31] D. Meggiolaro, E. Mosconi, F. de Angelis, *ACS Energy Lett.* **2018**, *3*, 447.
- [32] L. M. Herz, *ACS Energy Lett.* **2017**, *2*, 1539.
- [33] M. T. Weller, O. J. Weber, P. F. Henry, A. M. Di Pumpo, T. C. Hansen, *Chem. Commun.* **2015**, 51, 4180.
- [34] a) D. Meggiolaro, F. de Angelis, *ACS Energy Lett.* **2018**, *3*, 2206; b) H. Shahivandi, M. Vaezzadeh, M. Saeidi, *IEEE J. Photovolt.* **2020**, *10*, 1750.
- [35] P. Ramming, N. Leupold, K. Schötz, A. Köhler, R. Moos, H. Grüninger, F. Panzer, *J. Mater. Chem. C* **2021**, DOI: 10.1039/D1TC01554K .

Manuscript received: May 5, 2021

Revised manuscript received: June 14, 2021

Accepted manuscript online: June 16, 2021